Geophysical Research Letters

RESEARCH LETTER
10.1029/2019GL083120

An Integrated Geophysical Approach to Track Magma Intrusion: The 2018 Christmas Eve Eruption at Mount Etna

F. Cannavo'[1], M. Sciotto[1], A. Cannata[1,2], and G. Di Grazia[1]

[1]Istituto Nazionale di Geofisica e Vulcanologia, Osservatorio Etneo, Catania, Italy, [2]Dipartimento di Scienze Biologiche, Geologiche e Ambientali-Sezione di Scienze della Terra, Universitá degli Studi di Catania, Catania, Italy

Key Points:
- Integrated multiparametric geophysical investigation allowed to spatially and temporally track magma intrusion with unprecedented resolution
- Infrasonic source modeling permitted to reconstruct the effects on central plumbing system caused by the eruptive fracture opening

Supporting Information:
- Supporting Information S1
- Movie S1

Correspondence to:
F. Cannavo',
flavio.cannavo@ingv.it

Citation:
Cannavo, F., Sciotto, M., Cannata, A., & Di Grazia, G. (2019). An integrated geophysical approach to track magma intrusion: The 2018 Christmas Eve eruption at Mount Etna. *Geophysical Research Letters*, *46*. https://doi.org/10.1029/2019GL083120

Received 3 APR 2019
Accepted 26 JUN 2019
Accepted article online 8 JUL 2019

Abstract On 24 December 2018, a violent eruption started at Mount Etna from a fissure on the southeastern flank. The intrusive phenomenon, accompanied by intense Strombolian and lava fountain activity, an ash-rich plume, and lava flows, was marked by significant ground deformation and seismicity. In this work, we show how an integrated investigation combining high-rate GPS data, volcano-tectonic earthquakes, volcanic tremor, infrasound tremor, and infrasound events allows tracking the magma intrusion phenomenon spatially and temporally with unprecedented resolution. Moreover, it enabled showing how the central magma column lowered as a response to the flank eruption and to constrain the zone of interaction between the dike and the central plumbing system at a depth of 2–4 km below sea level. This is important for understanding flank and summit interaction, suggesting that explosive summit activity may in some cases be driven by lateral dike intrusions.

1. Introduction

On 24 December 2018, a violent eruption took place from a 2-km-long fissure opened on the southeastern flank of the volcano (Figure 1; Bonforte et al., 2019). The eruption, preceded by a 5-month-long period of moderate explosive activity and small lava flows at the summit craters (Laiolo et al., 2019), consisted of Strombolian and lava fountain activity from several vents along the fracture (reaching a minimum altitude of ~2,400 m a.s.l. (above sea level)) and minor explosive activity from the summit craters (especially Bocca Nuova, BN; New South-East Crater, NSEC; and North-East Crater, NEC). The eruption gave rise to a dense ash-rich plume and lava flows on the Valle del Bove. From the first moments, the relatively medium-low altitude of the effusive fracture prompted concerns for civil defense because of the hazards related to the opening of distal eruptive fissures (Bonaccorso et al., 2015). The explosive activity decreased markedly during the afternoon and ended during the night between 24 and 25 December, while the lava flows were fed up to 27 December.

In this work, we show how an integrated geophysical approach, combining high-rate GPS data, volcano-tectonic earthquakes, volcanic tremor, infrasound tremor, and infrasound events, allows tracking the magma intrusion phenomenon over time and space with unprecedented resolution. Furthermore, by exploiting the infrasound source modeling, we were able to provide information on the variations taking place in the central plumbing system at the same time as the lateral eruption.

2. Materials and Methods

In order to track the magma migration during the intrusion phenomenon, as well as to reconstruct the concomitant variations of the plumbing system feeding the central craters, video, GPS, volcano-tectonic earthquakes, volcanic tremor, infrasound tremor, and events acquired from 08:00 to 24:00 (all times reported here are Greenwich Mean Time) on 24 December 2018 were analyzed. To characterize infrasound-related variations, infrasound data included a wider time interval (23–25 December).

Regarding video data, following Gaudin et al. (2017), images acquired by ENT thermal camera (Figure 1), with sampling rate of 0.5 Hz, were used to show the temporal evolution of the maximum temperature in each frame row (Figures 2a and 2b).

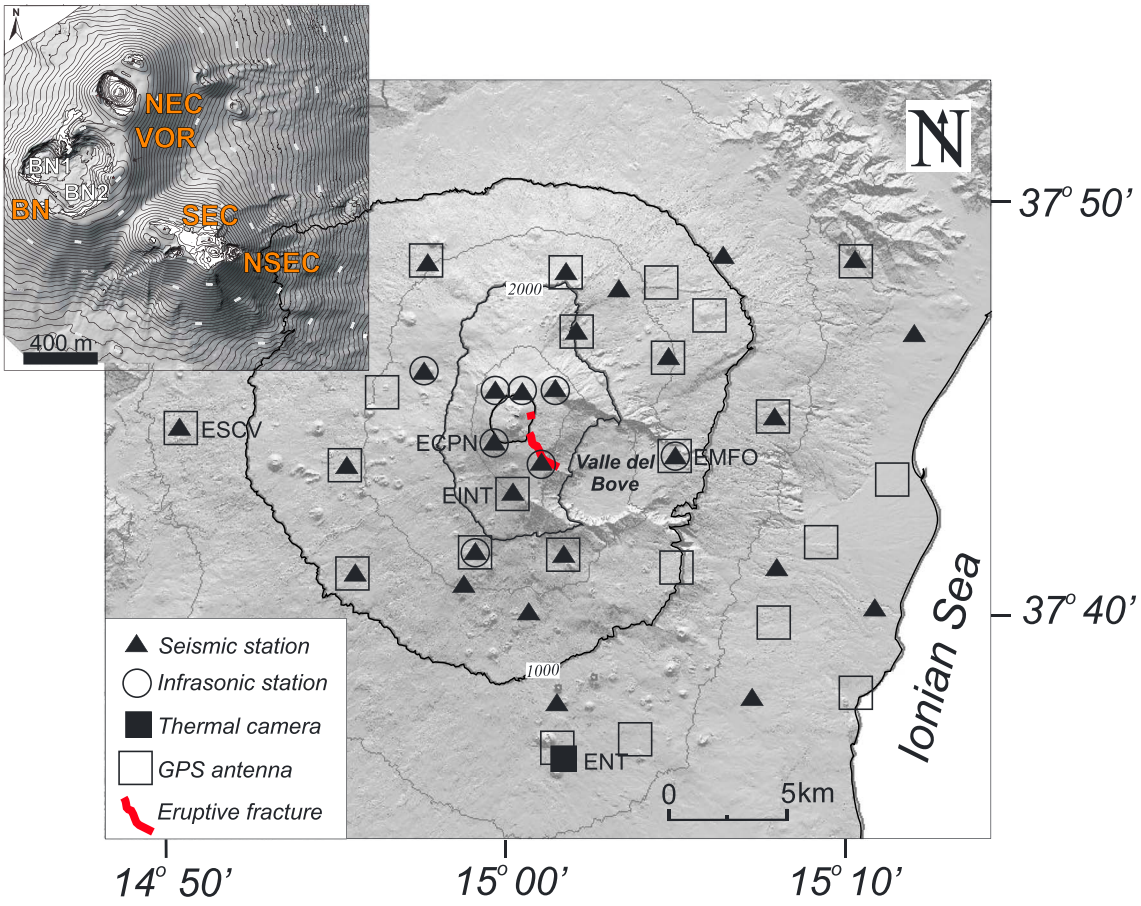

Figure 1. Digital elevation model of Mount Etna showing the locations of the sensors used in this work. The inset in the left upper corner shows the digital elevation model of the summit area (VOR, Voragine; BN, Bocca Nuova; NEC, North-East Crater; SEC, South-East Crater; NSEC, New South-East Crater; from Neri et al., 2017).

As for deformation, we used time series of positions of 21 GPS stations processed by GIPSY/OASIS 6.4 (Zumberge et al., 1997) in kinematic mode with a 5-min rate. Displacements were computed as the difference between the observed position at each time step and the position at 08:00 (see, e.g., Figure 2c). The dike was modeled with an Okada model (Okada, 1985), whose parameters were estimated by inverting the cumulative displacement field for 24 December 2018 (Figures 3a and 3b and Table S1 in the supporting information). To analyze the spatiotemporal evolution of the eruption, we patched the dike model (Figure 3b) in a matrix of 6 × 6 cells (each one of ~800 × 600 m in length × width). After solving for unit opening Green's functions for each patch, in order to suppress unrealistic scattered solutions, we added a spatial Laplacian and a second-order backward derivative (to preserve causal consistency) smoothing constraints to the inverse problem design matrix (Jonsson, 2002; Montgomery-Brown et al., 2010, see Text S1 for more details). The linear direct problem considered for the ground deformation source modeling is shown in the following equation:

$$\begin{bmatrix} d \\ 0 \end{bmatrix} = \begin{bmatrix} G \\ k_s\nabla^2 + k_t d^2/dt^2 \end{bmatrix} \theta + \varepsilon \tag{1}$$

where d is the vector of cumulative displacements on time, θ is the vector of the unknown model parameters (i.e., the patches openings on time), G is the matrix of Green's functions, and ε are the remaining errors. A nonnegative least squares inversion was used to solve for the dike-time-varying-opening model θ in equation (1).

The volcano-tectonic earthquakes were characterized by computing local magnitude (M_L), hypocentral location by the Hypoellipse (Hirn et al., 1991), and the 1-D velocity model (Hirn et al., 1991) and released energy by using the equation of seismic power (Dibble, 1974) assuming a seismic velocity of 2,500 m/s,

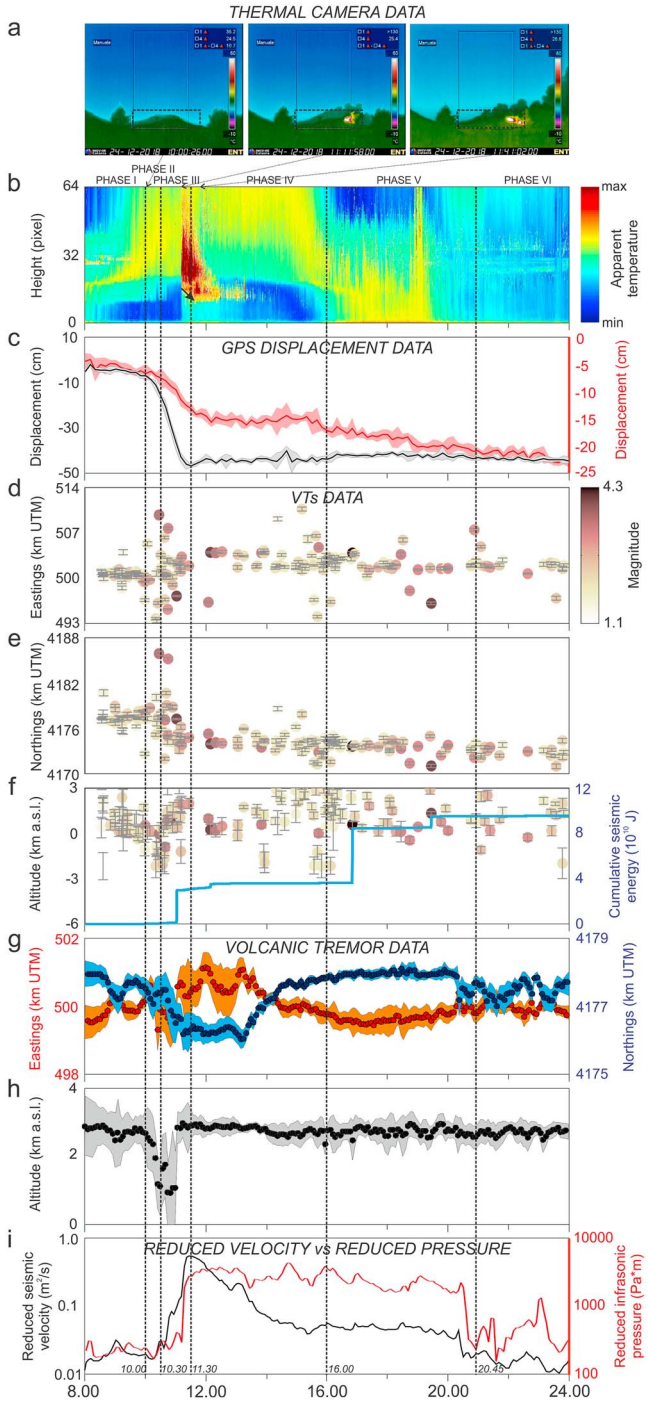

Figure 2. Time series from 08:00 to 24:00 on 24 December 2018. (a) Frames taken by ENT thermal camera. (b) Time/height diagram showing the evolution of the maximum temperature in each row of the portion of the frame, enclosed by the dashed rectangle in (a). The black arrow shows the downward migration of the eruptive vent along the fracture. (c) Displacement of east-west component of ECPN (black line) and EINT (red line) GPS stations. The red and gray areas show the band of error of the displacement. (d) Longitude, (e) latitude, and (f) altitude of the VT earthquake locations with the error bars. The color of the dots depends on the magnitude (see colorbar in (d)). The blue line in (f) indicates the variation in time of the cumulative seismic energy. (g) Longitude (red dots) and latitude (blue dots) of the tremor source centroid, with the associated errors (orange and blue bands). (h) Altitude of the volcanic tremor source centroid with the associated errors (gray band). (i) Seismic velocity reduced at 1 m from the volcanic tremor source (black line) and infrasonic pressure reduced at 1 m from the infrasonic source (red line). The vertical black dashed lines indicate the boundaries between the different phases represented in Figure 3.

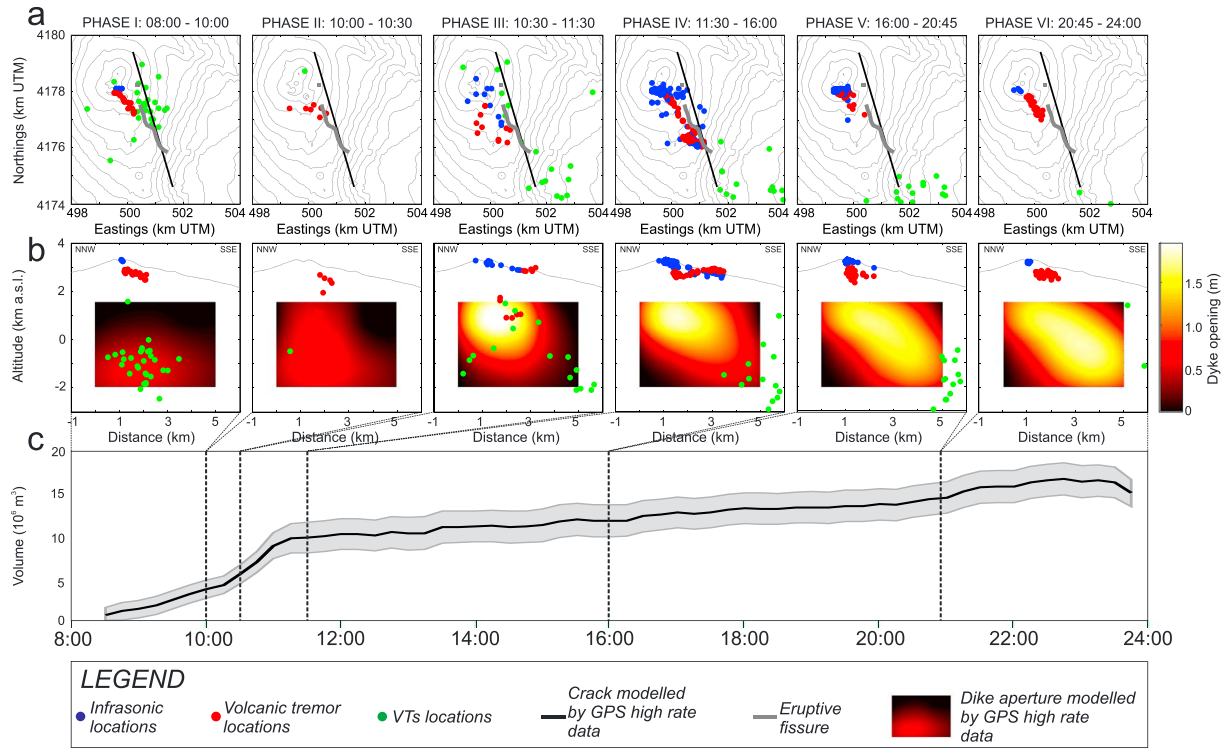

Figure 3. (a) Digital elevation model of Etna showing the locations of volcanic tremor centroids (red dots), infrasonic tremor and events (blue dots), volcano-tectonic earthquakes (green dots), the crack modeled by GPS data (black thick line), and the eruptive fissure (gray thick line) during six time intervals of 24 December 2018. (b) Section of Mount Etna along the dike direction showing the locations of volcanic tremor centroids (red dots), infrasonic tremor and events (blue dots), volcano-tectonic earthquakes (green dots), and the dike aperture modeled by GPS data (smoothed color scale) during six time intervals of 24 December 2018. (c) Cumulative volume calculated from the dike aperture with the associated error band (in gray).

applied on the signal recorded by ESCV (Figures 1, 2d–2f, 3a, and 3b). This time series of cumulative seismic energy shows sharp steps due to the earthquakes with the highest magnitudes, such as $M_L = 4.0$ at 11:01, $M_L = 4.3$ at 16:50, and $M_L = 4$ at 19:26 (Figure 2f). As for volcanic tremor, its dynamics was characterized by (Figures 2g–2i, 3a, and 3b): (i) source centroid locations, constrained by the grid search algorithm, developed by Di Grazia et al. (2006) and based on the spatial distribution of seismic amplitudes at 17 broadband seismic stations with a sampling rate of 100 Hz (Figure 1); (ii) reduced seismic velocity at 1 m from the source. Infrasound, recorded by eight microphones with flat response in 0.3–20,000 Hz and sampling rate of 50 Hz (Figure 1), was characterized by the following (Figures 2i, 3a, 3b, 4a–4c, and S2): (i) normalized spectrogram at EMFO station (Figure 1); (ii) source locations of both infrasound events and tremor by a grid search method based on the brightness function for the events and semblance function for tremor (Cannata et al., 2011, 2012); (iii) pressure reduced at 1 m from the source assumed to be at BN during 08:00–11:10, at the eruptive fissure during 11:11–13:30, and again at BN during 13:30–24:00.

To show in an integrated way the representative data together with the model outcomes and to follow the eruption dynamics, we edited an audiovisual available in the supporting information (Movie S1).

3. Results and Discussion

The period preceding the 24 December 2018 eruption was characterized by an almost constant rate of inflation, which started with the end of paroxysm sequence during 2011–2016 and was occasionally interrupted by episodic volcanic activities. We modeled the ground displacements measured by the GPS network during this long inflation (i.e., 2016–2018) phase with a finite spherical source (McTigue, 1987), located at about 8.3 km b.s.l. (below sea level) with a volume change of about $40 \cdot 10^6$ m^3 (see Table S1 for details).

On the morning of 24 December, a seismic swarm marked the beginning of a new eruption, characterized by distinct phases (Figures 2-4). Starting from 8:30, the swarm of low-magnitude volcano-tectonic earthquakes accompanied the beginning of dike intrusion hitting the shallow base of the volcano at about 2 km

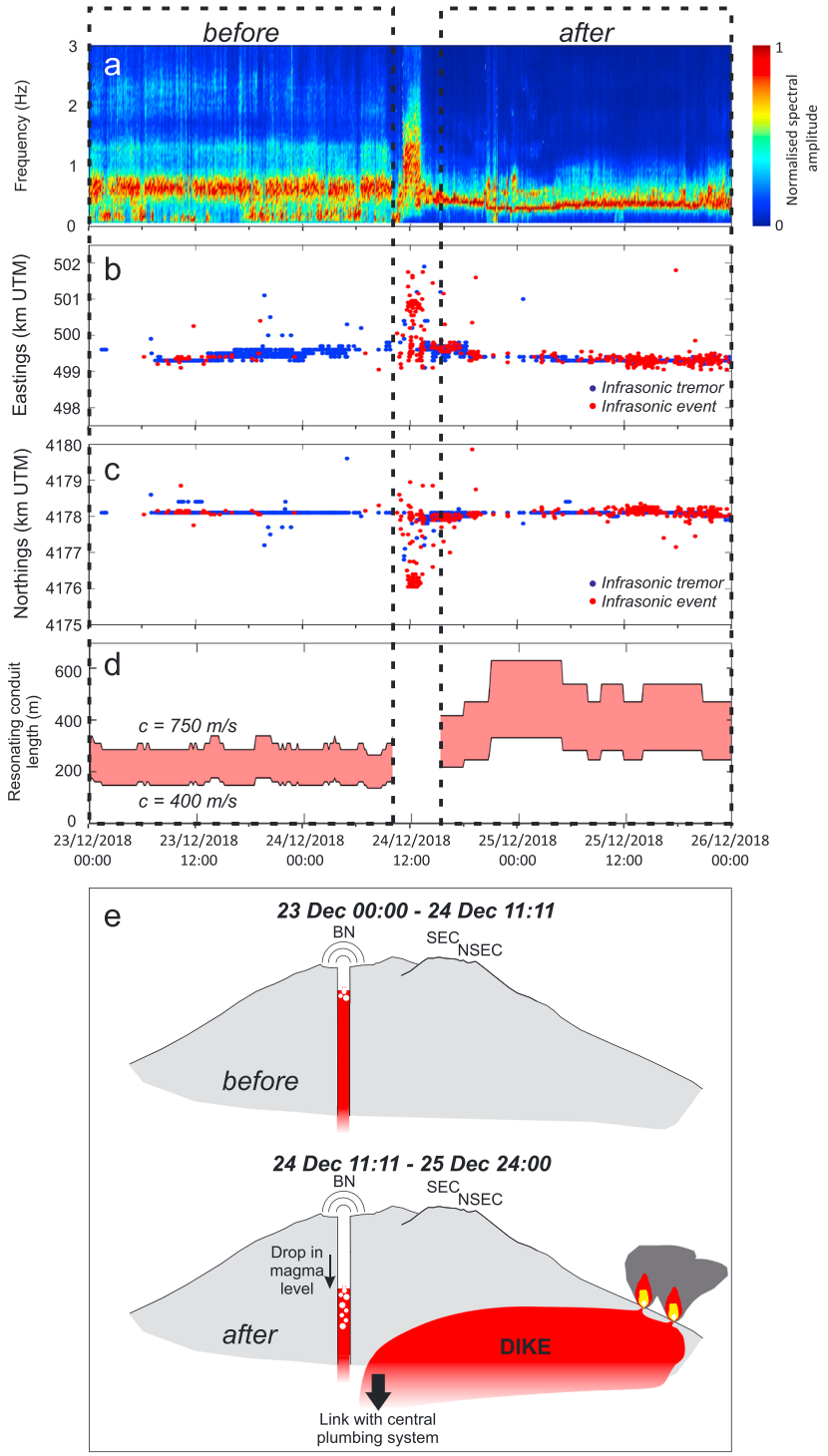

Figure 4. (a) Normalized spectrogram of the infrasound recorded by EMFO station from 23 to 25 December 2018. (b, c) Longitude and latitude of infrasonic tremor and events sources from 23 to 25 December 2018. (d) Length of the resonating portion of the conduit feeding BN, assuming a conduit radius equal to 12 m and the acoustic speed in the fluid into the conduit in the range 400–750 m/s. (e) Sketch of Mount Etna section showing the plumbing system feeding BN. It is shown how a drop in magma level took place within the BN conduit due to the opening of the eruptive fissure. *Before* and *after* in (a–d) indicate the two time intervals highlighted in (e).

b.s.l. Less than 1 hr later (~9:20), the summit GPS stations at the surface started to measure an appreciable ground deformation pattern (Figure 2c). From the detection of the ground displacement and till 1 hr after the beginning of the phenomenon (up to ~10:00), the dike opening onset, inferred by GPS data, was estimated to be confined in the same zone affected by volcano-tectonic earthquakes, between 0 and 2 km b.s.l. with a predicted volume of $3 \cdot 10^6$ m^3 (see Phase I in Figure 3c). The intrusion was also accompanied by migration of the volcanic tremor source centroid, as well as by its amplitude variations (Figures 2g–2i). In particular, up to ~10:00 the tremor source centroid was located at very shallow depth below the BN-NSEC area. Successively, at the same time as a gradual tremor amplitude increase, the centroid migrated at higher depth (down to ~1 km a.s.l.; see Phases II and III in Figures 2 and 3), suggesting the activation of a second deeper and more energetic tremor source. The deepest locations of this source coincide with the shallowest part of the dike modeled by GPS data. From ~10:00 to ~10:50, at the same time as the activation of this second tremor source, stronger displacements allowed us to infer the magma rising along the northwest part of the crack reaching the top of the modeled crack (1.7 km a.s.l.; see Phase II in Figures 2 and 3). The magma ascent velocity was estimated from the model at ~2 km/hr, in agreement with literature estimate of magma ascent rate (e.g., Rutherford, 2008; Petrelli et al., 2018). At ~11:10, accordingly with the southeastward migration of the tremor source centroid at shallower depth, a sharp opening in the uppermost part of the dike indicated that the magma was approaching to the surface at summit crater latitude. The analysis of thermal images shows that the eruptive fissure opened at the eastern base of NSEC at 11:11, and from 11:11 to ~11:35 (see black arrow in Figure 2b) a downward propagation of the eruptive vents took place in SSE direction (see Phase III in Figures 2 and 3). Such a first eruptive phase, characterized by the most intense explosive activity, was accompanied by the climax in the amplitude of both volcanic tremor and infrasound. As for the latter, at the same time as the opening of the eruptive fissure and the lava fountain development, a sharp increase of the reduced pressure occurred (Figure 2i). This infrasonic signal was located at the eruptive fissure (see Figures 3a, 3b, 4b, 4c, and S2 for details), and consisted of tremor and discrete events. The end of this intrusion was marked by the depletion of the ground displacements at ~12:00 and a subsequent decline in explosive activity from the fissure, as shown by the thermal camera in the early afternoon (~13:30; Figure 2b) together with the amplitude decrease in geophysical signals (volcanic tremor and infrasound). In detail, at ~13:30 together with the gradual decrease of volcanic tremor amplitude, the reduced pressure showed a slight decrease, and a few minutes later a further increase (Figure 2i), which was not related to the volcanic activity at the eruptive fissure, but rather to the low-frequency infrasonic tremor from BN (see Phases IV and V in Figures 2i, 3a, 3b, and 4a–4c). At ~14:30, the volcanic tremor source centroid migrated northwestward and was located again at shallow depth below the BN-NSEC area (see Phase IV in Figures 2 and 3). This suggests the weakening of volcanic tremor source related to the dike propagation and activity, that became gradually secondary, in terms of amplitude, with respect to the source located in the summit crater area. Starting from ~15:00, a number of low-magnitude earthquakes resumed striking the southern sector of Etna edifice, and in particular the upper southern rim of Valle del Bove (see Figure 1). In the meantime, the eruption continued with a mild and steady effusive activity from different vents along the eruptive fissure till ~16:00 when seismic and geodetic measurements indicated a further pulse of intrusion. Indeed, at that time, the swarm of volcano-tectonic earthquakes intensified in numbers and released energy (Figure 2f), and relevant displacements were measured by the GPS stations located in the southern sector of the volcano (Figure 2c). The space-time modeling explained this deformation pattern with a southward propagation of the dike. The crack propagated to the SSE at a depth between ~0 and 1 km b.s.l., in good agreement with the volcano-tectonic earthquake locations (see Phase V in Figures 3a and 3b). This dike propagation, taking place in the afternoon and highlighted by deformation and volcano-tectonic earthquake data, can be explained as an impairment of the southern and lower-altitude part of the volcano, already heavily stressed during the first intrusion. A sudden drop in the amplitude of volcanic tremor and infrasonic signals was recorded at ~20:45 (see Figure 2i Phases V–VI) when the maximum opening part of the dike finally moved southward, while the southward dike propagation waned only at ~22:00 and ceased the following day. It is worth noting that the measured seismic energy release, in agreement with the other data, outlined the two key phases: the shallow dike emplacement between 10:00 and 12:00 (see Phase III in Figure 2f) and the beginning of dike propagation from 16:00 (see Phase V in Figure 2f).

The total intruded volume has been estimated from the modeled dike aperture at $\sim 14 \cdot 10^6$ m^3 (Figure 3c). Although ground cracking was quite extensive, only a small volume of material was erupted. Most of this volume did not extrude as testified by preliminary observations, suggesting a total erupted volume of $\sim 1 \cdot 10^6$ m^3

(Laiolo et al., 2019). The low efficiency of the volcano in releasing the stored volumes is notable: from an estimated recharged volume of $40 \cdot 10^6$ m^3 only 35% (i.e., $14 \cdot 10^6$ m^3) of it was able to intrude, and even only 7% (i.e., $1 \cdot 10^6$ m^3) of the intruded volume reached the surface during this eruption.

The analysis of infrasound indicates that the dike intrusion affected the dynamics of the central plumbing system. The spectrogram of infrasound (Figure 4a) indicates a continuous volcanic infrasonic tremor during the considered time interval. As shown by the infrasonic locations (Figures 3a, 3b, 4b, 4c, and S2b), during the explosive activity (i.e. ~11:11–13:00), the tremor, with most energy between 0.5 and 2.0 Hz, was generated by the eruptive fracture, while before and after was emitted by BN. The spectral content of the BN tremor changed before and after the explosive phase: indeed, it had a frequency content of ~ 0.64 Hz before the eruption and ~ 0.34 Hz on average right after (Figure 4a). In particular, at around 21:00 and for about 12 hr, it reached the minimum frequency of 0.3 Hz. The energy radiated at frequencies <0.3 Hz before the eruption onset was not related to volcano activity but to both microbarom and wind noise. Infrasound radiation from BN during 24 December mainly consisted of discrete events and low-frequency tremor, which was characterized by high reduced pressure up to ~20:45 (Figure 2i).

The monochromatic signature of this infrasonic tremor emitted by BN before and after the eruption suggests mechanisms involving the resonance of portions of plumbing system, conduit and/or vent. Furthermore, the fact that this signal persisted, with the same frequency content, during different kinds of degassing/explosive phenomena at the vent are other factors supporting a path effect rather than a strictly source-related cause. Such a type of resonance-related generation mechanism of infrasound has been evoked by several authors to explain infrasonic emission from volcanoes (e.g., Kilauea: Fee et al., 2010; Villarica: Johnson et al., 2018; Etna: Spina et al., 2014; Cotopaxi: Johnson et al., 2018; Aso: Yokoo et al., 2019). In the light of these resonance models, changes in the plumbing systems were inferred based on the temporal variations of the infrasonic frequencies (Etna, Sciotto et al., 2013; Spina et al., 2014; Villarrica, Richardson et al., 2014; Johnson et al., 2018). In the case of the 24 December 2018 Etna eruption, the decrease of the peak frequency of the infrasonic tremor from ~0.64 to ~0.34 Hz can be interpreted as resulting from an increase in the resonator dimension. We assume that the pipe-like resonator is the portion of the conduit, filled with a gas mixture and comprised between the free magma surface (closed termination) and the crater rim (open termination). To avoid the increase of unknown resonator parameters, we assumed a simple cylindrical geometry of the conduit. To model the length of the resonating portion of the conduit (L), we applied the following equation (e.g., Kinsler, 2000; Johnson et al., 2018):

$$L_{\text{eff}} = L + \frac{8}{3\pi}a = \frac{c_i}{4f_p} \tag{2}$$

where L_{eff} is the effective pipe length, function of both conduit length (L) and radius (a), c_i is the acoustic speed in the fluid into the conduit, and f_p is the fundamental resonance frequency. The radius of the conduit was considered in the range 4–20 m (Rymer et al., 1995; Vergniolle & Ripepe, 2008). The acoustic speed in a fluid is given by the root square of the heat capacity ratio (γ), the gas constant (R), and the temperature (T) of the fluid. To constrain the acoustic speed into the conduit, we used chemical compositions of gas emitted by central craters (La Spina et al., 2010) and applied the ideal mixing theory (Morrissey & Chouet, 2001). The obtained speed values, considering T equal to 300, 800, and 1200 K, and R and γ values for each gas species (Morrissey & Chouet, 2001; Serway & Jewett, 2005), range between 400 and 750 m/s. Considering an average value of the acoustic speed (575 m/s), the increase of the resonator length after the eruption was ~200 m (Figure S1) with an uncertainty of about 10 m, associated with the conduit radius. Likewise, the magma-free level inside the conduit of BN crater deepened from about 215 to 415 m below the crater rim (for a 12-m conduit radius). Such a variation, suggesting a drop in the magma level inside the central plumbing system, is consistent with the opening of the eruptive fissure at low altitude and the consequent effective magma drainage (see Figure 4e). This is also a further evidence of the link between the eruptive fissure and the central plumbing system. A similar drop in magma level in the central plumbing system, due to the hydraulic connection with a lateral vent/fissure, was observed at Mount Etna during the 2008–2009 eruption (Spina et al., 2014). Furthermore, at Kilauea Patrick et al. (2019) showed how during the 2010–2011 fissure opening, events at the East Rift Zone regulated summit activity at distances of 20 km. If we consider an altitude of the inner part of BN of 3,200 m a.s.l. (Neri et al., 2017), the altitude of the magma-free level inside the BN conduit should be 2,800 m a.s.l. after the eruption onset, higher than the eruptive vents along the fracture (minimum altitude of ~2,400 m a.s.l.). Following Patrick et al. (2019), such an altitude difference

could be related to either the lower density of the magma in the central plumbing system (due to greater gas content) or to the incomplete summit draining, taking time to reach equilibrium. Another evidence of volcano summit-flank pairing, even if at shallower depth, has recently been provided by Ripepe et al. (2015) on Stromboli flank eruptions/plumbing system.

From the spatiotemporal modeling, since the dike ascent propagated vertically decentralized from the central craters at a depth of 2 km b.s.l. (Figure 3b), the interaction between the central plumbing system and dike intrusion had to happen at least at a depth equal or higher than 2 km b.s.l., consistent with the common magma deflation sources feeding the central craters located below 4 km b.s.l. (Aloisi et al., 2018). An upward migration/intrusion of magma along a NNW-SSE structural trend was also inferred for the 1991–1993, 2001, and 2002–2003 lateral eruptions (Alparone et al., 2012, and references therein) and the 13 May 2008 eruption (Aloisi et al., 2009).

It is worth noting that most of the considered geophysical signals measured deviations from their normal values up to 2.5 hr before the opening of the fissure at the surface (Figure 2). This confirms the reliability of the volcano monitoring tools in sensing the changing volcanic status. The volcanic tremor centroid changed its position right after the first earthquakes that likely opened a path for the dike ascent. This was confirmed 1 hr later not only by a deepening of its location but also by the ground deformation data which, increasing their signal-to-noise ratio, showed a clear intrusive pattern. The inversion of deformation data in accordance with the earthquake and volcanic tremor locations clearly defined in time the dike geometry and position even before the evidence of the eruptive fractures. The information coming from the different kinds of geophysical data are complementary though partially overlapped: GPS and volcano-tectonic earthquakes permitted tracking the dike intrusion from depth up to the volcano surface; volcanic tremor allowed identifying and locating the shallowest part of the intruding dike; infrasound tracked the explosive activity, in terms of explosivity and eruptive vent locations.

4. Conclusions

On 24 December 2018, an eruption, accompanied by one of the most intense ground deformation and volcano-tectonic activity since 2002, took place at Mount Etna. The main findings of the multiparametric investigation of the very first day of the eruption are as follows: (i) It has been possible to track the dike intrusion from its early stage at depths of ~2 km b.s.l. and during its propagation; (ii) Geophysical data have allowed us to constrain the location and geometry of the dike and its dynamical parameters. Indeed, we calculated a magma ascent rate of ~2 km/hr, a minimum intruded volume of $\sim 14 \cdot 10^6$ m^3. We have shown that, despite the significant seismic and geodetic energy released, the efficiency of this eruption in terms of ratio between erupted and intruded volumes of magma is quite low; (iii) Thanks to the infrasound data, it has been possible to detect and quantify the interaction between the dike and the central plumbing system, and, by the geodetic modeling, to constrain the likely depth of this interaction between 2 and 4 km b.s.l.

The joint analysis of all the considered kinds of data and their interpretation through models has allowed us to image the spatiotemporal dynamics of the intrusion leading to the eruption with unprecedented detail.

Acknowledgments
Gruppo Analisi Dati Sismici of Istituto Nazionale di Geofisica e Vulcanologia, Osservatorio Etneo-Sezione di Catania is kindly acknowledged for providing volcano-tectonic earthquake data. We are indebted to the technicians of the INGV, Osservatorio Etneo for enabling the acquisition of seismic, infrasonic, GPS, and video data. A. C. thanks "Piano Triennale della Ricerca di Dipartimento 2016-18-seconda annualitá," id 22722132140 (Project Coordinator M. Viccaro). We thank the Editor Rebecca Carey, the reviewer Matt Patrick, and an anonymous reviewer for their critical reading of the manuscript and constructive comments, which helped us to improve the manuscript. We thank Stephen Conway for revising and improving the English language of the text. The volcano-tectonic earthquake data are available in http://www.ct.ingv.it/ufs/analisti/catalogolist.php. In agreement with the INGV data policy, the other geophysical data are available from the authors as follows: GPS data, flavio.cannavo@ingv.it; volcanic tremor data, giuseppe.digrazia@ingv.it; infrasonic data, mariangela.sciotto@ingv.it.

References

Aloisi, M., Bonaccorso, A., Cannavò, F., & Currenti, G. M. (2018). Coupled short- and medium-term geophysical signals at Etna volcano: Using deformation and strain to infer magmatic processes from 2009 to 2017. *Frontiers in Earth Science*, *6*, 109. https://doi.org/10.3389/feart.2018.00109

Aloisi, M., Bonaccorso, A., Cannavò, F., Gambino, S., Mattia, M., Puglisi, G., & Boschi, E. (2009). A new dyke intrusion style for the Mount Etna May 2008 eruption modelled through continuous tilt and GPS data. *Terra Nova*, *21*(4), 316–321. https://doi.org/10.1111/j.1365-3121.2009.00889.x

Alparone, S., Barberi, G., Cocina, O., Giampiccolo, E., Musumeci, C., & Patané, D. (2012). Intrusive mechanism of the 2008–2009 Mt. Etna eruption: Constraints by tomographic images and stress tensor analysis. *Journal of Volcanology and Geothermal Research*, *229-23*, 50–63. https://doi.org/10.1016/j.jvolgeores.2012.04.001

Bonaccorso, A., Calvari, S., & Boschi, E. (2015). Hazard mitigation and crisis management during major flank eruptions at Etna volcano: Reporting on real experience. *Geological Society, London, Special Publications*, *426*(1), 447–461. https://doi.org/10.1144/sp426.4

Bonforte, A., Guglielmino, F., & Puglisi, G. (2019). Large dyke intrusion and small eruption: The December 24, 2018 Mt. Etna eruption imaged by sentinel-1 data. *Terra Nova*. https://doi.org/10.1111/ter.12403

Cannata, A., Grazia, G. D., Aliotta, M., Cassisi, C., Montalto, P., & Patanè, D. (2012). Monitoring seismo-volcanic and infrasonic signals at volcanoes: Mt. Etna case study. *Pure and Applied Geophysics*, *170*(11), 1751–1771. https://doi.org/10.1007/s00024-012-0634-x

Cannata, A., Sciotto, M., Spampinato, L., & Spina, L. (2011). Insights into explosive activity at closely-spaced eruptive vents using infrasound signals: Example of Mt. Etna 2008 eruption. *Journal of Volcanology and Geothermal Research*, *208*(1-2), 1–11. https://doi.org/10.1016/j.jvolgeores.2011.09.003

Di Grazia, G., Falsaperla, S., & Langer, H. (2006). Volcanic tremor location during the 2004 Mount Etna lava effusion. *Geophysical Research Letters*, *33*, L04304. https://doi.org/10.1029/2005GL025177

Dibble, R. R. (1974). Volcanic seismology and accompanying activity of Ruapehu Volcano, New Zealand, *Developments in solid earth geophysics* (pp. 49–85). Amsterdam: Elsevier. https://doi.org/10.1016/B978-0-444-41141-9.50009-7

Fee, D., Garcés, M., Patrick, M., Chouet, B., Dawson, P., & Swanson, D. (2010). Infrasonic harmonic tremor and degassing bursts from Halema'uma'u Crater, Kilauea Volcano, Hawaii. *Journal of Geophysical Research*, *115*, B11316. https://doi.org/10.1029/2010JB007642

Gaudin, D., Taddeucci, J., Scarlato, P., del Bello, E., Ricci, T., Orr, T., et al. (2017). Integrating puffing and explosions in a general scheme for Strombolian-style activity. *Journal of Geophysical Research: Solid Earth*, 1860–1875. https://doi.org/10.1002/2016JB013707

Hirn, A., Nercessian, A., Sapin, M., Ferrucci, F., & Wittlinger, G. (1991). Seismic heterogeneity of Mt Etna: Structure and activity. *Geophysical Journal International*, *105*(1), 139–153. https://doi.org/10.1111/j.1365-246X.1991.tb03450.x

Johnson, J. B., Ruiz, M. C., Ortiz, H. D., Watson, L. M., Viracucha, G., Ramon, P., & Almeida, M. (2018). Infrasound tornillos produced by volcán Cotopaxis deep crater. *Geophysical Research Letters*, *45*(11), 5436–5444.

Johnson, J. B., Watson, L. M., Palma, J. L., Dunham, E. M., & Anderson, J. F. (2018). Forecasting the eruption of an open-vent volcano using resonant infrasound tones. *Geophysical Research Letters*, *45*, 2213–2220. https://doi.org/10.1029/2018GL077766

Jonsson, S. (2002). Fault slip distribution of the 1999 M_w 7.1 Hector Mine, California, earthquake, estimated from satellite radar and GPS measurements. *Bulletin of the Seismological Society of America*, *92*(4), 1377–1389. https://doi.org/10.1785/0120000922

Kinsler, L. (2000). *Fundamentals of acoustics*. New York: Wiley.

La Spina, A., Burton, M., & Salerno, G. G. (2010). Unravelling the processes controlling gas emissions from the central and northeast craters of Mt. Etna. *Journal of Volcanology and Geothermal Research*, *198*(3-4), 368–376. https://doi.org/10.1016/j.jvolgeores.2010.09.018

Laiolo, M., Ripepe, M., Cigolini, C., Coppola, D., Schiava, M. D., Genco, R., et al. (2019). Space- and ground-based geophysical data tracking of magma migration in shallow feeding system of Mount Etna volcano. *Remote Sensing*, *11*(10), 1182. https://doi.org/10.3390/rs11101182

McTigue, D. F. (1987). Elastic stress and deformation near a finite spherical magma body: Resolution of the point source paradox. *Journal of Geophysical Research*, *92*(B12), 12931. https://doi.org/10.1029/JB092iB12p12931

Montgomery-Brown, E. K., Sinnett, D. K., Poland, M., Segall, P., Orr, T., Zebker, H., & Miklius, A. (2010). Geodetic evidence for en echelon dike emplacement and concurrent slow slip during the June 2007 intrusion and eruption at Kılauea volcano, Hawaii. *Journal of Geophysical Research*, *115*, B07405. https://doi.org/10.1029/2009jb006658

Morrissey, M. M, & Chouet, B. A (2001). Trends in long-period seismicity related to magmatic fluid compositions. *Journal of Volcanology and Geothermal Research*, *108*(1-4), 265–281. https://doi.org/10.1016/s0377-0273(00)00290-0

Neri, M., Maio, M. D., Crepaldi, S., Suozzi, E., Lavy, M., Marchionatti, F., et al. (2017). Topographic maps of mount Etna's summit craters, updated to December 2015. *Journal of Maps*, *13*(2), 674–683. https://doi.org/10.1080/17445647.2017.1352041

Okada, Y. (1985). Surface deformation due to shear and tensile faults in a half-space. *Bulletin of the Seismological Society of America*, *75*(4), 1135–1154.

Patrick, M., Orr, T., Anderson, K., & Swanson, D. (2019). Eruptions in sync: Improved constraints on Kılauea volcanos hydraulic connection. *Earth and Planetary Science Letters*, *507*, 50–61. https://doi.org/10.1016/j.epsl.2018.11.030

Petrelli, M., Omari, K. E., Spina, L., Guer, Y. L., Spina, G. L., & Perugini, D. (2018). Timescales of water accumulation in magmas and implications for short warning times of explosive eruptions. *Nature Communications*, *9*(1), 770. https://doi.org/10.1038/s41467-018-02987-6

Richardson, J. P., Waite, G. P., & Palma, J. L. (2014). Varying seismic-acoustic properties of the fluctuating lava lake at Villarrica volcano, Chile. *Journal of Geophysical Research: Solid Earth*, *119*, 5560–5573. https://doi.org/10.1002/2014JB011002

Ripepe, M., Donne, D. D., Genco, R., Maggio, G., Pistolesi, M., Marchetti, E., et al. (2015). Volcano seismicity and ground deformation unveil the gravity-driven magma discharge dynamics of a volcanic eruption. *Nature Communications*, *6*(1), 6998. https://doi.org/10.1038/ncomms7998

Rutherford, M. J. (2008). Magma ascent rates. *Reviews in Mineralogy and Geochemistry*, *69*(1), 241–271. https://doi.org/10.2138/rmg.2008.69.7

Rymer, H., Cassidy, J., Locke, C. A., & Murray, J. B. (1995). Magma movements in Etna volcano associated with the major 1991–1993 lava eruption: Evidence from gravity and deformation. *Bulletin of Volcanology*, *57*(6), 451–461. https://doi.org/10.1007/bf00300989

Sciotto, M., Cannata, A., Gresta, S., Privitera, E., & Spina, L. (2013). Seismic and infrasound signals at Mt. Etna: Modeling the north-east crater conduit and its relation with the 2008–2009 eruption feeding system. *Journal of Volcanology and Geothermal Research*, *254*, 53–68. https://doi.org/10.1016/j.jvolgeores.2012.12.024

Serway, R. A., & Jewett, J. W. (2005). *Principles of physics: A calculus-based text Edited by* Thomson. Belmont, CA: Brooks Cole.

Spina, L., Cannata, A., Privitera, E., Vergniolle, S., Ferlito, C., Gresta, S., et al. (2014). Insights into Mt. Etna's shallow plumbing system from the analysis of infrasound signals, August 2007-December 2009. *Pure and Applied Geophysics*, *172*(2), 473–490. https://doi.org/10.1007/s00024-014-0884-x

Vergniolle, S., & Ripepe, M. (2008). From Strombolian explosions to fire fountains at Etna volcano (italy): What do we learn from acoustic measurements? *Geological Society, London, Special Publications*, *307*(1), 103–124. https://doi.org/10.1144/sp307.7

Yokoo, A., Ishii, K., Ohkura, T., & Kim, K. (2019). Monochromatic infrasound waves observed during the 2014–2015 eruption of Aso volcano, Japan. *Earth, Planets and Space*, *71*(1), 12. https://doi.org/10.1186/s40623-019-0993-y

Zumberge, J. F., Heflin, M. B., Jefferson, D. C., Watkins, M. M., & Webb, F. H. (1997). Precise point positioning for the efficient and robust analysis of GPS data from large networks. *Journal of Geophysical Research*, *102*(B3), 5005–5017. https://doi.org/10.1029/96jb03860